International Journal of Hydrogen Energy 87 (2024) 890–901

Contents lists available at ScienceDirect

International Journal of Hydrogen Energy

journal homepage: www.elsevier.com/locate/he

In-situ surface activation of polycrystalline $LaNiO_3$ electrocatalyst for the oxygen evolution reaction

Giuditta De Amicis [a], Anna Testolin [b], Cristina Cazzaniga [b], Francesco D'Acapito [c], Alessandro Minguzzi [d,e,f,*], Paolo Ghigna [a,d], Alberto Vertova [d,e]

[a] Dipartimento di Chimica, Università di Pavia, Viale Taramelli 16, 27100, Pavia, Italy
[b] Industrie De Nora S.p.A., Via Leonardo Bistolfi 35, 20134 Milan, Italy
[c] CNR-IOM-OGG LISA-CRG c/o ESRF, 71 Avenue des Martyrs, Grenoble, France
[d] Istituto Nazionale di Scienza e Tecnologia dei Materiali, via Giusti 9, Firenze, Italy
[e] Dipartimento di Chimica, Università degli Studi di Milano, Via Golgi 19, 20133, Milan, Italy
[f] Dipartimento di Energia, Politecnico di Milano, Via Lambruschini, 4a - 20156, Milano, Italy

ARTICLE INFO

Handling Editor: Prof I Tolj

Keywords:
Alkaline water electrolysis
Oxygen evolution reaction
Surface disorder
Polycrystalline $LaNiO_3$
Operando X-ray absorption

ABSTRACT

The efficiency of hydrogen production from water electrolysis is limited by the sluggish kinetics of the Oxygen Evolution Reaction (OER), necessitating catalytic material to avoid the high overpotentials. This study investigates $LaNiO_3$ as a promising electrocatalyst for the OER in Alkaline Water Electrolysis selected for its cost-effectiveness and easy scale-up. $LaNiO_3$, prepared by a co-precipitation method, shows good OER activity and electrochemical stability. *Operando* X-Ray Absorption Spectroscopy (XAS), reveals a crucial role of the Ni(II)/Ni (III) redox couple. Notably, a layer of a Ni(II) compound formed at the catalyst surface is oxidized under anodic potentials and possibly becomes the active sites for the adsorption of OH^- and for the OER reaction. High resolution transmission electron microscopy confirms the formation of a defective outer layer during operation, indicating the presence of disordered structure on the surface of the electrocatalyst, which increases the number of active sites for the OER.

1. Introduction

Hydrogen, as an energy carrier, could have a key role in a clean, secure, and affordable energy for the future. However, at the moment, hydrogen production is dominated by reforming of natural gas [1], gasification of coal and petroleum coke [2], or gasification and reforming of heavy oil [3]. Recently, different sources of hydrogen production have coded with colors. *Black*, *grey* or *brown* refer to the production of hydrogen from coal, natural gas and lignite respectively [4]. *Blue* is commonly used for the production of hydrogen by steam methane reforming with Carbon Capture Utilization and Storage (CCUS), using natural gas or biomass [5]. *Green* is a term applied to production of hydrogen from water by electrolysis using electricity from renewable energy sources. At present, only 4% *ca.* of the global hydrogen supply is green [6]. Overall, water electrolysis is limited by the sluggish electrode kinetics associated with the Oxygen Evolution Reaction (OER) at the anode [7,8], rather by the cathodic hydrogen evolution reaction (HER). This is due to OER, which involves a four-electron transfer, compared to two-electron transfer for the HER [9,10]. The overall change in free energy, for the four electrons water splitting reaction, amounts to 4.92 eV [11]. In this situation, the ideal anodic material would require a potential of 1.23 V (vs RHE). For now, IrO_2 and RuO_2 are the most efficient catalysts for OER, but are extremely expensive, as Ir and Ru are two of the least abundant elements on the earth [12–14]. It is also well-known that these oxides are the most active and stable noble metal in acidic electrolytes [15], but are not equally stable in alkaline ones [16,17].

Operating in alkaline (basic) conditions, in principle, permits the use of non-noble and low-cost metal electrocatalysts [18,19], leading to the possibility of cheaper hydrogen production [20]. Numerous studies [21–25] have already shown the high catalytic activity of nickel oxide electrocatalyst in alkaline electrolytes applicable in electrolysers, and the research of this class of materials is still ongoing, as demonstrated by the most recent literature. For example, Ni-doped CoP encapsulated by B- and N- co-doped carbon (Ni–CoP/BNC) electrocatalysts synthetized by hydrothermal synthesis, followed by a thermal treatment [26] and a

* Corresponding author. Istituto Nazionale di Scienza e Tecnologia dei Materiali, via Giusti 9, Firenze, Italy.
E-mail address: alessandro.minguzzi@unimi.it (A. Minguzzi).

https://doi.org/10.1016/j.ijhydene.2024.09.038
Received 11 April 2024; Received in revised form 30 August 2024; Accepted 3 September 2024

novel core-shell heterostructure that involves 1D $NiMoO_4$ nanorod core and 2D $Co(OH)_2$ nanosheet shell, which function as bifunctional electrocatalysts for the oxygen evolution reaction (OER) via a facile two-step method [27].

In the present work, we studied the perovskite $LaNiO_3$ as a catalytic material for anodic in Alkaline Water Electrolysis (AWE). Among several perovskite oxides, $LaNiO_3$ is one of the most promising candidate due to its low charge transfer resistance, high conductivity and good electrocatalytic properties for OER [28,29]. Furthermore, among several perovskite oxides, $LaNiO_3$ is particularly promising due to its favorable electrocatalytic kinetic and grater performance for OER, ranking among the best-performing in terms of activity between perovskites in the pure state [30].

$LaNiO_3$ has the intrinsic activity for OER because of its single electron-filled e_g orbital on Ni^{3+} at B-site [31]. In turn, this allows a favorable bond energy for surface (B-site)-O bonding in OER [32]. Perovskite oxides have an ideal cubic structure with stoichiometry ABO_3 in which lanthanides or alkaline earth cations occupy the A-site, and transition metal cations the B-site. Lanthanides and transition metals are highly abundant elements, which allows the purchase of bulk materials for industrial processes [33]. Their flexible crystal and electronic structure provide them ideal candidates to study the correlations between OER activity and structure [34,35]. An indispensable step for studying electrocatalysis is the investigation of the surface composition of the transformed surface that indicated a strong correlation between OER activity and surface composition [36].

One of the most important aspects to study in OER electrocatalysis is the accessibility of active sites, related to the possibility of ion diffusion through the active layer [37], that is related to the hydrous/amorphous *vs* crystalline nature of the material. The increased performances (and instability) of hydrous materials, compared to "crystalline" was evidenced on several OER electrocatalysts and particularly on IrO_2 [38–43]. In parallel, the formation of amorphous/hydrated layers in the outer portion of the electrocatalyst surface was observed in many cases [34,44,45].

For what concerns $LaNiO_3$, Baeumer et *al.* determined the tunability of surface transformation of $LaNiO_3$ epitaxial thin films showing that the Ni termination is considerably more active than the La termination, and that this difference originates from a thermodynamically stable, Ni oxyhydroxide-type single-layer (disordered) surface phase NiO_2 which forms during the operation of Ni-terminated surfaces and is kinetically inaccessible when starting with a La termination [46].

This interesting finding prompted us to investigate on this phenomenon but on $LaNiO_3$ electrodes synthetized with a scalable method, which can be applied at the industrial level. In particular, we adopted a synthesis based on a co-precipitation method followed by calcination at 700 °C [47]. The powder was then fully characterized by structural, morphological and electrochemical probes. We also adopted *operando* X-ray absorption spectroscopy (XAS), aiming at better understanding of the reaction mechanisms in the case of the OER on $LaNiO_3$ anodes, an approach that we have already adopted with other electrode and photoelectrode materials [48–53]. In fact, XAS has now become an essential tool for the study of charge state, local geometry and electronic structure of specific elements (nickel in this case) during the occurrence of physico-chemical phenomena [54]. This technique allows for a deeper understanding of the real active sites involved in these processes [55].

We observed the formation of a disordered layer on the surface polycrystalline $LaNiO_3$ electrocatalyst combining XAS, high resolution transmission electron microscopy (HR-TEM), cyclic voltammetry and quasi-steady state polarization curves. Specifically, we demonstrated that, under sufficiently cathodic conditions, a layer of a Ni(II) compound is formed at the catalyst surface, that is then reversibly oxidized under anodic potentials forming Ni(III) sites at the surface, that possibly become the active sites for the adsorption of the reagent and the subsequent OER reaction. The number of active sites increase during operation thus increasing the active area of the electrocatalyst, i.e. the number of exposed Ni centers.

Similar observations have recently been made for Co-MOF electrocatalysts, showing that the electroactivation of the composite requires the involvement of the OER. This process leads to a remarkable increase in the electroactive population of cobalt centers [56].

It seems therefore that reaching the right crystallinity degree is one of the possible pathways to reach a high activity/high stability material for the OER. In other words, it is one of the possible approaches to apply the so-called "rational design" of a catalyst [57].

Still, we need further information in the field, and this is at the bases of the present work, where we succeeded in the study of the polycrystalline $LaNiO_3$ system as electrocatalyst for the OER, evidencing the beneficial contribution of its surface disorder for water splitting reaction in alkaline media.

2. Materials and methods

2.1. Synthesis of lanthanum nickel oxide

$LaNiO_3$ was synthesized by a co-precipitation method [47], as previously reported [58]. Briefly, 0.01 mol of $La(NO_3)_2{\cdot}6H_2O$ (puriss. p.a., ≥99.0% tritation, Fluka) and 0.01 mol of $Ni(NO_3)_2{\cdot}6H_2O$ (99.999% trace metals basis, Aldrich) were dissolved in deionized water (Milli-Q) and stirred at room temperature until complete dissolution. Then, a solution of 2 M KOH was dropped-in slowly, up to pH ≥ 13. After the formation of a precipitate, it was washed with deionized water until neutral pH, and finally dried thanks to Buchner filtration. After that, the powder was put in an oven in air at 60 °C for 3 h. Finally, the perovskite powder was obtained after a calcination step in a muffle furnace at 700 °C for 3 h in air.

2.2. Structural and morphological characterization

Phase composition and crystal structure of $LaNiO_3$ was checked by X-ray diffraction (XRD). The XRD pattern was recorder with a Multi-Purpose Diffractometer (Panalytical X'Pert PRO MPD) using a Cu anode (K_α radiation, $\lambda = 1.5405$ Å). The crystalline phases have been identified using the ICDD (International Center for Diffraction Data) database. Rietveld refinement of the experimental diffraction was carried out [58].

Moreover, SEM analysis to check surface morphology and the chemical composition of the catalyst were performed using a SEM-FEG Inspect F-50 instrument, with secondary electrons image working with a distance of 10 mm and a high tension from 10 kV to 20 kV.

High resolution transmission electron microscopy (HR-TEM) was carried out using a FEI Tecnai F20 a Field Emission Gun (FEG, probes <3 nm) to confirm the particle size and in particular to study the surface behavior of perovskite and its changes.

2.3. Electrochemical characterizations

The OER performance of the synthesized material was studied in a three-electrode cell set up using a Rotating Disk Electrode (RDE) from Pine instruments and Autolab (PGSTAT30 – EcoChemie, The Netherlands) potentiostat. The thin-film RDE approach reported in Ref. [59] was followed. The Working Electrode (WE) was a perovskite-modified glassy carbon, the Reference Electrode (RE) was a mercury/mercury oxide (Hg/HgO – internal solution 1 M KOH) and the Counter Electrode (CE) was a Platinum wire as these are experiments to study the OER. Prior to the experiments, the WE glassy carbon surface was polished with the #4000 SiC paper and demineralized water. Then, 2 mg mL^{-1} of catalyst ink was prepared by weighing a selected amount of $LaNiO_3$, in a mixture of 1:4 Milli-Q water:isopropanol (C_3H_7OH). Nafion® Dupont was used as a binder in a ratio of 0.1w/w Nafion: catalyst. Then the mixture was ultrasonicated for 30 min. After that, 20 μL of the ink were deposited by drop casting on the WE (surface 0.196

cm^2) to ensure a catalyst load of 200 μg cm^{-2}.

All the RDE electrochemical characterizations were performed following the procedure reported in Ref. [58]. The measured potentials were corrected for the ohmic-drop measured by Krastjic and Trasatti method [60].

The $LaNiO_3$ catalyst was also characterized using Screen-Printed Carbon Electrodes,C-SPE, Metrohm DropSens Electrode 110. The substrate is ceramic-based and is3.38 cm long, 1.02 cm wide, and 0.05 cm thick. The WE, RE and CE are made of carbon, silver and carbon, respectively. The WE diameter is 4 mm corresponding to an area of 0.1256 cm^2.

52 μL of the $LaNiO_3$ ink, the same adopted for RDE analysis, was deposited by drop casting on the carbon WE. The SPE was then dipped in 1 M KOH supporting electrolyte solution. In this work, we preferred not to use the CE and RE present on the SPE, particularly for the small area of the CE, compared to the much higher surface area of the deposited powder and for the poorer definition of the reference potential of a pseudo-Ag reference electrode. We therefore opted for using external electrodes, a Pt wire, and a silver/silver chloride (Ag/AgCl) in 3 M aqueous KCl as the counter and reference electrode, respectively. For C-SPE measurements, the pre-conditioning step of the catalyst layer was the same as for the RDE protocol. After that, a series of CV curves in the potential range 0.5–2 V (vs RHE) at 5 mV s^{-1} in 1 M KOH were recorded. Thus, a total amount of 0.1 mg of $LaNiO_3$ has been deposited on Carbon surface, obtaining a Ni concentration of 0.2 mg cm^{-2}.

To evaluate the catalyst stability in the electrochemical cell for XAS experiment, the activity towards the OER was determined as follows. NaOH is used for XAS experiments because sodium absorbs less X-rays than potassium. For this reason, all the robustness experiments were performed using 1 M NaOH. 0.4 mL of the $LaNiO_3$ ink, used previously for RDE and C-SPE analysis, was deposited by drop casting on a 1 cm^2 glassy carbon electrode (WE). An Ag wire was used as pseudo-RE and a Pt lamina as CE. The electrochemical cell was the same used for *operando* XAS experiment described in *paragraph 2.4)* and showed in Fig. 1 (panel B). Even in this case, the same pre-conditioning step of the catalyst layer, used in the RDE protocol, was performed. Due to the long times required for XAS experiments, the material stability under OER conditions was tested by recording 10,000 CVs between 1.4 and 1.9 V (vs RHE) at 1 V s^{-1}. Before and after, CVs at a lower scan rate, 5 mV s^{-1}, were recorded and compared.

All the measured currents were converted to current densities and all the potentials values were converted versus RHE.

2.4. Operando XAS experiment

For the detection of Ni oxidation state and possible variations thereof, *operando* X-Ray absorption spectroscopy (XAS) experiments were carried out at the nickel K-edge at room temperature in the fluorescence mode at the *Linea Italiana di Spettroscopia di Assorbimento* (LISA) beamline (BM08) [61] at the European Synchrotron Radiation Facility (ESRF). The energy resolution of this beamline is *ca.* 0.1 eV at 8 keV [61].

A Si(111) fixed exit double crystal monochromator was used; the harmonic rejection and focusing was realized by Si mirrors with a cutoff energy of 15 keV. In particular, the first mirror (cylindrical) is a collimator permitting to obtain a quasi-theoretical energy resolution from the monochromator (~1.5 eV at the Ni–K edge) whereas the second toroidal mirror is used to focus the beam down to a dimension of about 100 μm on the sample. A high-purity germanium fluorescence detector array (12 elements) was used for measuring the fluorescence from the sample. The energy calibration was performed by measuring the absorption spectrum of metallic nickel foil at the Ni K-edge. The energy stability of the monochromator was checked by measuring the absorption spectrum of the Ni foil several times during the experiment. All data were obtained at room temperature. Spectra of NiO and β-NiOOH were acquired in the transmission mode and used as standards for the Ni(II) and Ni(III) oxidation states, respectively [62]. For those measurements, an appropriate amount of sample (to give a unit jump in the absorption coefficient) was mixed with cellulose and pressed into a pellet. A customized electrochemical cell was designed to ensure both electrochemical and XAS experiments [54]. The cell was designed and built using a 3D printer with a hollow-PTFE rectangular shape. The cell was equipped with an upper external part that allowed to hold RE and CE, respectively. A frontal circular hollow window of 0.196 cm^2 was created to ensure illumination by X-Ray, where the Working Electrode was placed. An Ag wire was used as RE, a Pt lamina as CE and a perovskite-modified Glassy Carbon (GC) as WE. The set-up is shown in Fig. 1.

All the experiments were performed using a 1 M sodium hydroxide solution (NaOH, Sigma Aldrich) serving as supporting electrolyte. An O-ring was used to prevent any solution leak. One glassy carbon electrode (WE) was modified with $LaNiO_3$ via drop casting (following the same ink preparation procedure reported in *paragraph 2.3*), with a Ni load of 0.2 mg cm^{-2}. The surface was activated as described in *paragraph 2.3)*. The activated surface was then placed facing the electrolyte in the cylinder, with the back side touching the circular hole. The X-Ray beam impinged at the back of the sample, passing through the glassy carbon electrode: this has been maintained thin enough (0.5 mm) to ensure a support

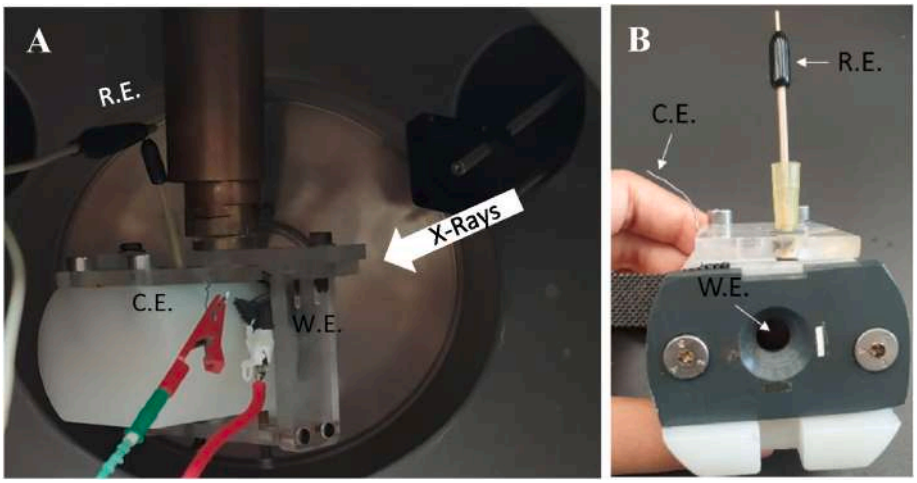

Fig. 1. Customized spectro-electrochemical cell for XAS experiments with three electrode setup: **A)** synchrotron setup and **B)** frontal view with circular hollow window where the Working Electrode (WE) was placed.

negligible X-Ray absorption at the Ni K-edge. The oxidation state of nickel was evaluated by recording a series of X-Ray Absorption Near Edge Structure (XANES) spectra at different fixed potential values, selected from previous electrochemical characterization. The selected values were: 0.16 V–0.96 V – 1.3 V–1.4 V – 1.46 V–1.6 V (vs RHE). For the XANES analysis, the raw spectra were first background subtracted with a straight-line fitting to the pre-edge, and then normalized to unit absorption at 800 eV above the edge energy, where the EXAFS oscillations are no longer visible. The EXAFS (extended X-ray absorption fine structure) were first extracted by means of the Athena code [63–65], and then the data analysis was performed by using the EXCURVE code, using a k^2 weighting scheme and full multiple scattering calculations.

3. Results and discussion

3.1. Synthesis of lanthanum nickel oxide

$LaNiO_3$ was synthetized with co-precipitation method, which is a simple and inexpensive method. This technique obeys industrial requirements and criteria in terms of low cost and ease scale-up. The efficiency of this approach was validated by measuring the structural and morphological properties through appropriate characterization analysis.

3.2. Structural and morphological analysis

The crystalline structure and phase composition of the $LaNiO_3$ was determined by XRD (see Fig. 2). The sample is almost monophasic, as it is shown by comparison with a standard pattern of rhombohedral $LaNiO_3$ (ICDD N° 04-013-6811) shown by the green vertical lines in Fig. 2. The presence of a weak peak at *ca.* a 44° can be ascribed to a small impurity of rock salt NiO [66].

The refinement of the experimental diffraction pattern of $LaNiO_3$ was obtained by the Rietveld method using the General Structure and Analysis Software (GSAS-II). The results of the analysis are reported in Table 1.

The determined unit cell parameters and the unit cell volume are in accordance with the standard unit cell parameters: a = b = 5.4596 Å, c = 13.1421 Å and volume = 339.3 $Å^3$.

Fig. 3 represents the SEM images of the $LaNiO_3$ and highlights the perovskite morphology. At low magnification the sample appears as formed by agglomerates and flakes. Pictures collected at higher magnifications reveal that the agglomerates are formed by particles with nanometric dimensions.

A comprehensive investigation of the surface behavior of the perovskite was carried out using high resolution electron transmission microscopy (HR-TEM). The investigation was done on the *as prepared* perovskite, on the material kept in 1 M KOH overnight, and on the same material after having worked under OER conditions. This three-step investigation allows to correlate the intrinsic properties of the material with its variations after the OER.

The HR-TEM images reveal that the perovskite $LaNiO_3$ *as prepared* exhibits a geminate periodicity, highlighted in red in Fig. 4A. The structure is remarkably homogeneous, leading to the observed periodicity that continues up to the edge, as evident in Fig. 4B. These nanocrystals demonstrate consistency, characterizing the whole structure, without any evidence of amorphous or disordered regions. The particles maintain their crystalline nature up to the edge. Fig. 4C shows the HR-TEM image of the $LaNiO_3$ that was kept in 1 M KOH overnight. Also in this case, the particles appear to be almost single domain, without any significant evidence of disorder near the surface. This confirms that crystal morphology is not affected by the contact with the electrolytic solution.

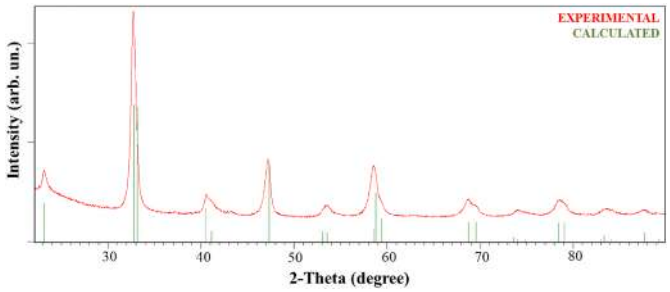

Fig. 2. Powder XRD pattern of $LaNiO_3$.

Conversely, in the $LaNiO_3$ OER, a significant amount of disorder near the surface is found, as depicted in Fig. 5. In this case, we found the formation of nano-domains (highlighted in the red boxes) near the surface, the dimension of each nano-domain being of the order of 3–4 nm. Here, the surface shows a high level of defectivity, resembling a mosaic structure rather than a single crystal.

After the electrochemical treatment, the gemination has not increased, as it is a characteristic of the bulk material. On the other hand, the disorder confined to the surface is only observed in the $LaNiO_3$ OER powder. As shown in Fig. 5B, the exterior appears disordered, while going inward (highlighted in the red box), larger particles remain continuous (a feature present in the bulk even in the $LaNiO_3$ *as prepared*). It is evident that, after the OER, disoriented nanoparticles formed or grew on the surface. The fact that after treatment overnight in 1 M KOH, the morphology of the perovskite is unchanged confirms that this increasing disorder is caused by the electrochemical reaction.

3.3. Electrochemical activity assessment

The OER performance of $LaNiO_3$ electrode, determined using RDE, is shown in Fig. 6. The perovskite catalyst shows a good OER activity, since the OER starts at ca. 1.63 V (vs RHE). The onset potential is calculated as the intersection of the tangent at the inflection point.

The potential E(V) value at 10 mA cm^{-2} is chosen as the metric OER catalyst: 10 mA cm^{-2} is the current density that approximately corresponds to the solar spectrum for an efficiency of 10 % under 1 solar illumination [67]. At this current density, the overpotential is 0.43 V, that is close the values reported while benchmarking OER electrocatalysts [16,17]. At this current density, the overpotential is 0.43 V, that is close the values reported while benchmarking OER electrocatalysts [68]. The same references reported overpotentials equal to 0.32 and 0.29 in aqueous 1 M NaOH for IrO_2 and RuO_2, respectively.

Comparing the over-potential at 10 mA cm^{-2} of the investigated perovskite with that of other pure perovskite oxides-based electrocatalysts on glassy carbon electrode [30] it can be noted that $LaNiO_3$ has the lowest over-potential value. This implies that, among several perovskite oxides, $LaNiO_3$ stands out as one of the most promising candidate due to its good electrocatalytic properties for OER and favorable electrocatalytic kinetics.

The Tafel slope for the $LaNiO_3$ electrode was determined by fitting the linear portion of the Tafel plots (Fig. 7a) using Equation (1).

$$\eta = \pm \ln 10 \frac{RT}{\alpha F} \log \frac{j}{j_0} = a + b \log j \quad (1)$$

where j is the current density, j_0 is the exchange current density and b is the Tafel slope [69]. The Tafel slope of 47 mV·dec^{-1} and the j_0 of $1.06 \cdot 10^{-9}$ A cm^{-2} are in excellent agreement with the literature for what concerns $LaNiO_3$ anodes [70]. The Tafel slope indicates how fast the current increases against overpotential (η), which means that a small Tafel slope, as in our case, suggests good electrocatalytic kinetics [69]. In addition, the Tafel slope of 47 mV·dec^{-1} (that is that is sufficiently close to 2RT/3F, equal to 40 mV·dec^{-1}), suggests that the rate determining step (rds) is a one-electron transfer electrochemical step, for example, an $EE_{rds}C$ [71].

$$S + OH^- \rightarrow S\text{–}OH + e^-$$

Table 1
Rietveld refinement of $LaNiO_3$.

Space Group	Structure	a/Å	b/Å	c/Å	Volume/Å^3	Crystallite Size/nm
R - 3c	Rhombohedral $LaNiO_3$	5.4469	5.4469	13.1948	339.030	23.9

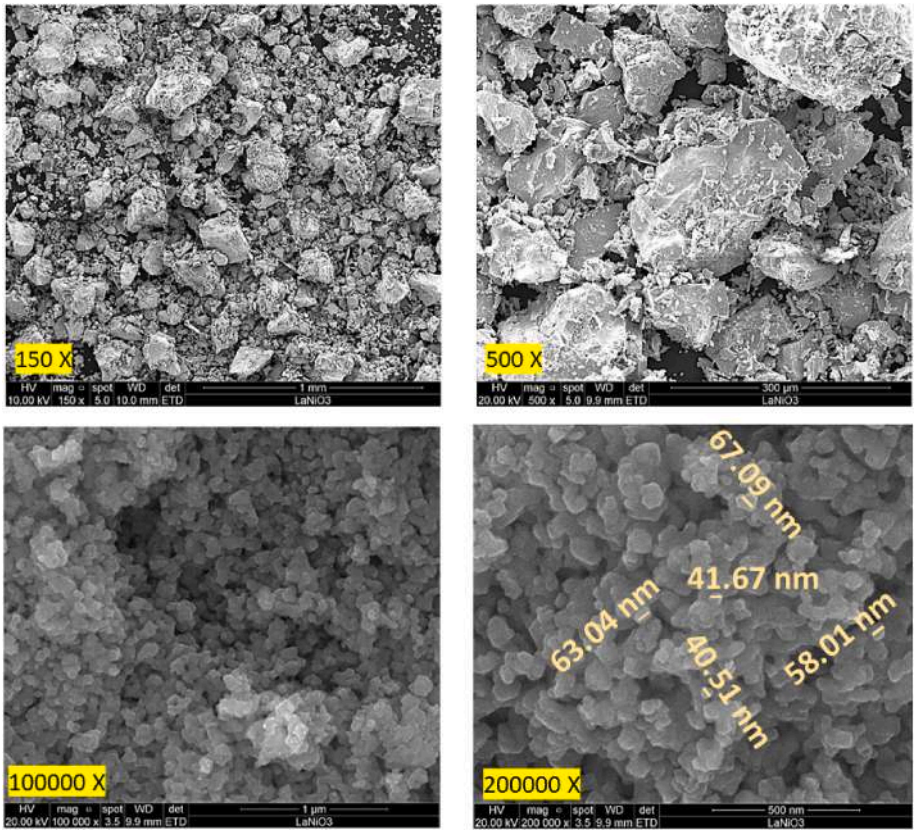

Fig. 3. SEM images showing the surface morphology and particles distribution of $LaNiO_3$.

$$S\text{–}OH + OH^- \rightarrow S\text{–}O + H_2O + e^-$$

$$2S\text{–}O \rightarrow 2S + O_2$$

or an ECE_{rds} [72]:

$$S\text{–}O + OH^- \rightarrow S\text{–}OOH + e^-$$

$$S\text{–}OOH + OH^- \rightarrow S\text{-}OO^- + H_2O$$

$$S\text{-}OO^- \rightarrow S + O_2 + e^-$$

Where S is the active site.

We also compared the Tafel slope with that of the IrO_2 electrode at pH 14 (1 M NaOH) from our previous paper [68], as presented in Fig. 7a with line blue. It can be observed that the slope for IrO_2 (48.8 mV·dec^{-1}) is comparable to that of our perovskite $LaNiO_3$. This confirms that the material is highly active for the OER, considering that IrO_2 is commonly used as benchmark electrocatalyst for this reaction,

In Fig. 7b the turnover frequency (TOF) is also shown with a orange line, as it is used to evaluate the morphological effect on the electrocatalyst's performance toward OER [73,74]. Additionally, we also compared the TOF with that of the IrO_2 electrode at pH 14 (1 M NaOH) from our previous paper [68] (Fig. 7b line blue). Although a better quantification of the number of active sites should be required [75], we estimated the TOF according to the following equation:

$$TOF = \frac{jA}{4nF} \tag{2}$$

where j represents the current density, A is the surface area of the electrode, F is the Faraday constant and n is the number of moles of Ni (III) reacted [76].

The cyclic voltammogram performed using C-SPE with 0.025 mg of nickel deposited is shown in Fig. 8; cathodic and anodic peaks are visible at about 1.3 V and 1.4 V (vs RHE), respectively. These peaks can be attributed to the Ni(II)/Ni(III) redox and are related to the oxidation/reduction of $Ni(OH)_2$/NiOOH couple [77]. The percentage of Ni moles reacting can be calculated, using equation (3), via peak integration, equation (2). A value of $1.6{\cdot}10^{-5}$ A V and $1.1{\cdot}10^{-5}$ A V were found for anodic and cathodic peak areas, respectively.

$$\mathrm{mol\,(Ni)_{reacted}} = \frac{\mathrm{Peak\,Area\,(A{\cdot}V)}}{\mathrm{scan\,rate\,(V{\cdot}s^{-1})}\cdot\mathrm{Faraday\,Constant\,(96485.31\,C/1mole^-)}} \tag{3}$$

$$\%\ \mathrm{mol\,(Ni)\ active\ in\ the\ reaction} = \frac{\mathrm{mol\,(Ni)_{reacted}}}{\mathrm{mol\,(Ni)_{tot}}} \tag{4}$$

The amount of nickel on electrode surface was calculated from the stoichiometry of the deposited perovskite.

The fraction of active Ni is about 8.3%, using the anodic peak area, and about 6%, using the cathodic peak area.

A series of 60 cyclic voltammetry measurements were carried out to

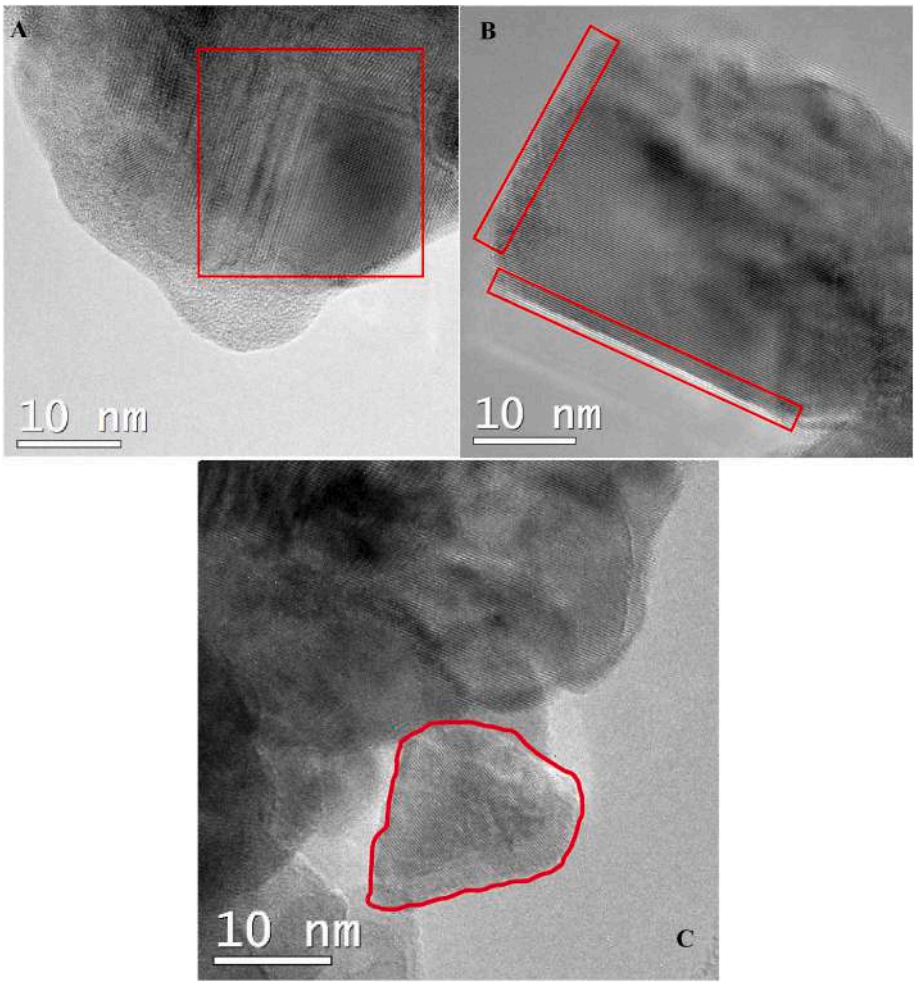

Fig. 4. HR-TEM images of $LaNiO_3$ *as prepared* (A and B) and after treatment in 1 M KOH (C).

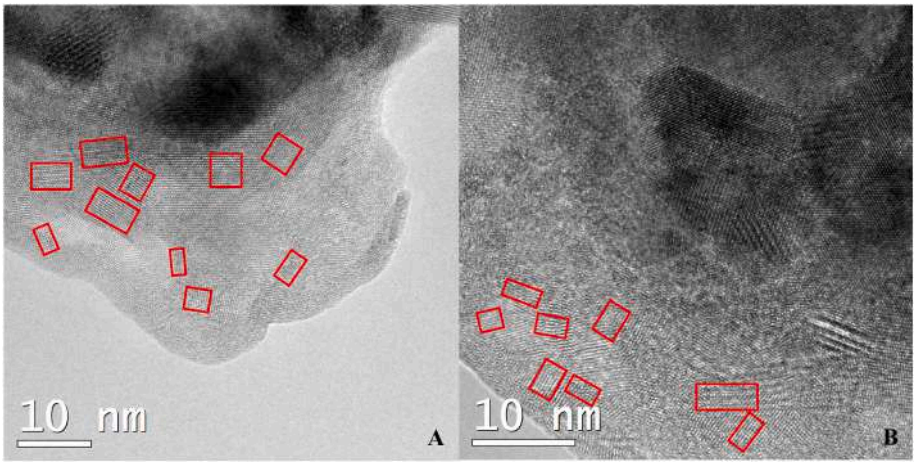

Fig. 5. HR-TEM images of $LaNiO_3$ after OER.

determine the progressive activation of the perovskite $LaNiO_3$ (Fig. 9a). It is observed that there is a discernible and gradual enhancement of both oxidation Ni(III) and reduction Ni(II) peaks with increasing number of cycles. As can be seen from Fig. 9b, the value of peak current density increases with higher cycles. In particular, it doubles after 60 cycles, indicating that the material electrochemical activity significantly increases during operation. The increase of peak current occurs for both the anodic and the cathodic scans, demonstrating that the increase of redox transition kinetics (and so, of the number of sites involved in this process) are reversible.

This experimental evidence confirms that the electrochemical treatment is responsible for activating the material, making it more capable for electrons and ion transfers. This analysis supports the HR-TEM investigation, pointing to the operando increase of the active

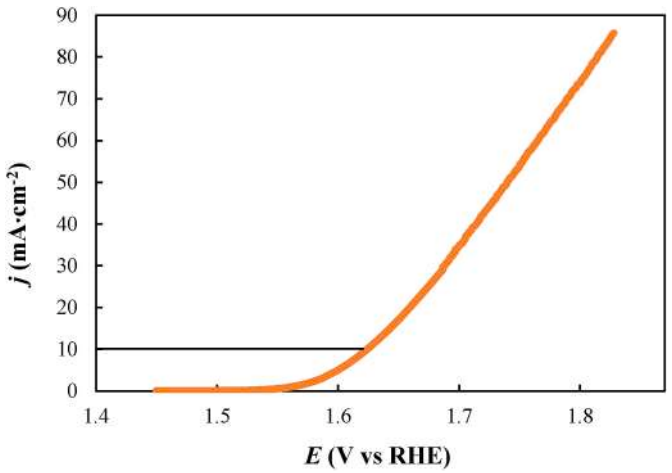

Fig. 6. Anodic scan of $LaNiO_3$ at 5 mV s^{-1} in 1 M KOH.

area, due to the fact that the material surface becomes disordered after the powder is subjected to electrochemical phenomena, either the redox transition between 1.2 and 1.4 V or the OER.

3.4. Operando X-ray absorption experiments

To verify the mechanical and chemical stability of the deposits, which requires to be stable for several hours during XAS experiments, we performed stress tests, cycling the deposited electrocatalytic powder in 1 M NaOH for 10,000 cycles at 1 V s^{-1} between 1.4 V and 1.9 V vs RHE. Fig. 10A shows the first and subsequent intermediate cycles during the stress test. These results illustrate the initial activation of the material, particularly observed at the 4,500th cycle, confirming that the electrochemical treatment induces the activation of the electrocatalyst. As the test progresses, the material loses part of its activity while converging to a stable situation.

Fig. 10B shows a comparison of the anodic semi-cycles before (orange curve) and after (green curve) the stress test lowering the scan rate to 5 mV s^{-1}. A weak electrochemical deactivation can be observed after 10,000 cycles, due to a small visible powder loss from the glassy carbon surface and found in the electrolyte after the experiment.

In conclusion, the system is sufficiently stable for the timing of the XAS experiment; the OER activity is still good after 10,000 cycles and there are no significant problems due to the bubbles formation. Taken together, these results confirm the effectiveness of the electrochemical treatment in activating the material and underline the durability and reliability of the system over extended cycles.

The XAS experiment results at the Ni K-edge on the $LaNiO_3$ material are shown in Fig. 11. In Fig. 11A, we first show the XANES spectrum of the pristine material, along with the corresponding derivative (Fig. 11B). The spectra of NiO and β-NiOOH are shown as references for the Ni(II) and Ni(III) oxidation states, respectively.

The exact edge energy position in XAS is a measure of the effective nuclear charge. This is due to the fact that the edge energy is the binding energy of a core electron (the Ni 1s electron in the present case). This binding energy is in turn due to the electrostatic interaction between the electron and the nucleus. This interaction is screened by the outer (valence) electrons. This screening means that the effective nuclear charge sensed by the electron is less than the formal nuclear charge. Now, an increase (say) of the oxidation state means that the number of outer electrons is decreased, the screening is lesser and the effective nuclear charge is increased. As a consequence, the edge energy position shifts towards higher energy with increasing oxidation state. Of course, the opposite effect is observed when decreasing the oxidation state. Thus, the edge energy position is used for an exact determination of the oxidation states of elements in materials. This effect is known as the chemical shift in XAS. It is apparent by comparison with the XANES spectra of the reference materials, that for the pristine material the edge energy position is coincident with that of β-NiOOH, which is a standard for Ni(III), and this allows to assign the mean oxidation state of Ni to Ni (III).

The XANES spectra of the materials under operando conditions are reported in Fig. 11C where a comparison is made of the spectrum of the pristine material with that of the material at 0.16 V, and then in all the

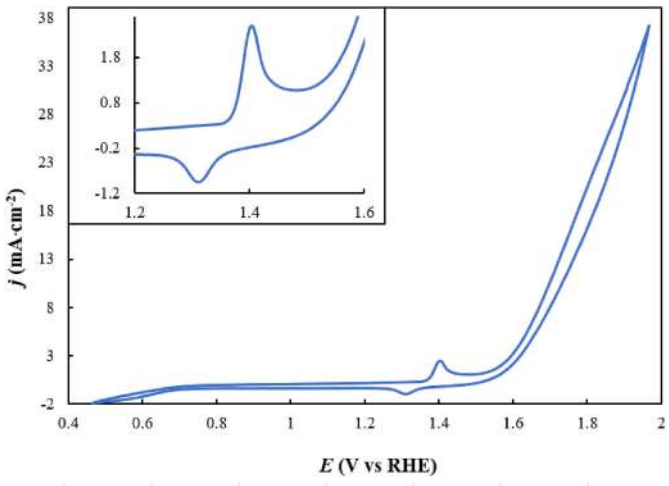

Fig. 8. Cyclic voltammogram of $LaNiO_3$ done with Screen-Printed Carbon Electrodes at 5 mV s^{-1} in 1 M KOH.

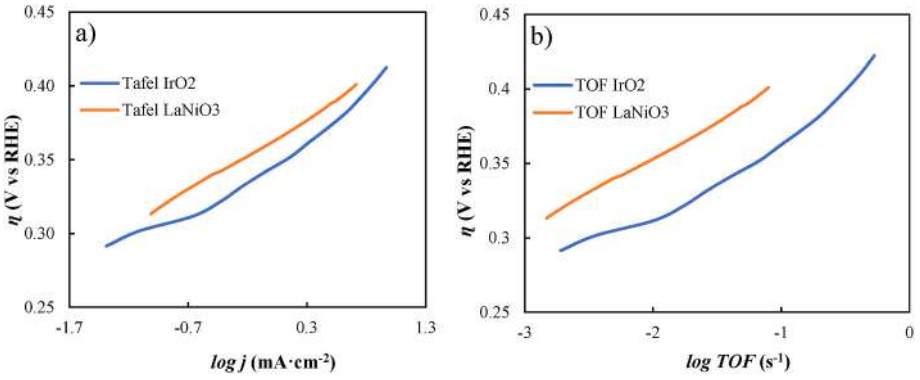

Fig. 7. In **a)** Tafel plot of $LaNiO_3$ (η vs log j) compared with that of IrO_2 from our previous paper [68]. In **b)** the calculation of the TOF (η vs log *TOF*) for $LaNiO_3$ is presented, again compared with that of IrO_2 from our previous paper [68]. Data for IrO_2 are reproduced from Ref. 60 with permission from the Royal Society of Chemistry.

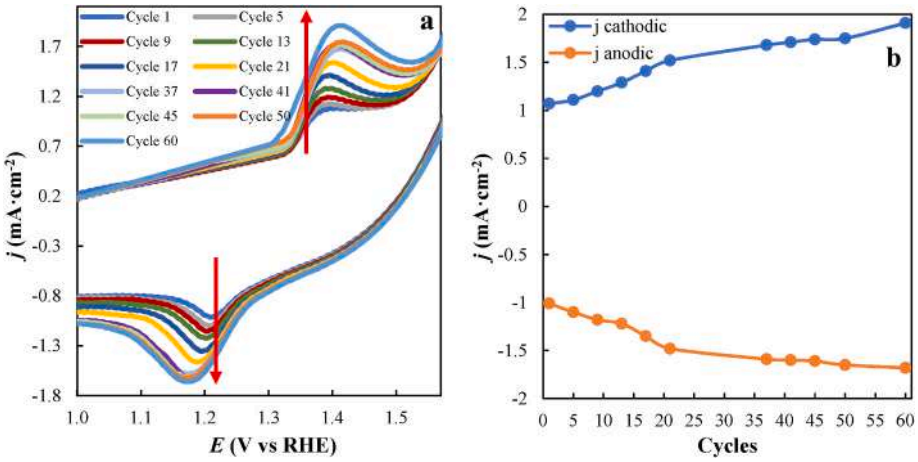

Fig. 9. In a) 60 cyclic voltammograms of $LaNiO_3$ at 50 mV s^{-1} in 1 M KOH: clear evidence of the progressive growth of oxidation (Ni^{3+}) and reduction (Ni^{2+}) peaks with increasing the number of cycles. In **b)** the trend of the anodic and cathodic peak current for all the cycles reported in **a)**.

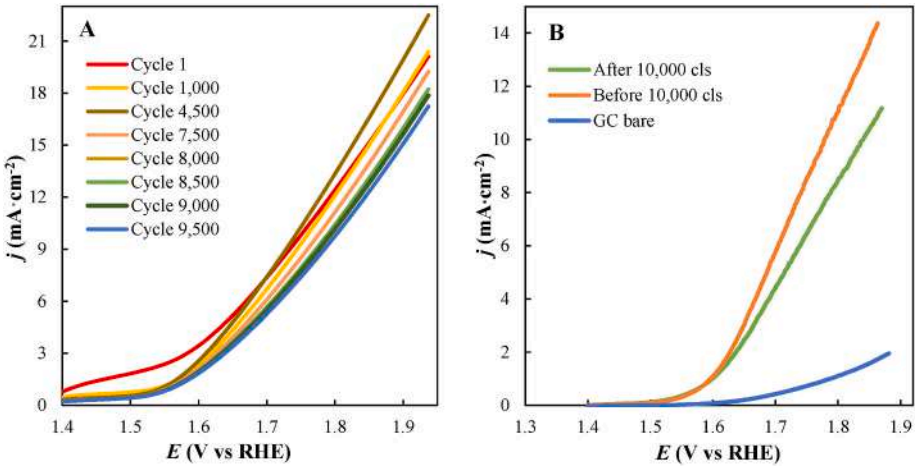

Fig. 10. A) Anodic curves (first and subsequent intermediate cycles) of $LaNiO_3$ in 1 M NaOH at 1 V s^{-1} during the stress test. **B)** Anodic scan, before and after the stress test, of $LaNiO_3$ in 1 M NaOH at 5 mV s^{-1} to evaluate the catalyst robustness.

other conditions in Fig. 11D (enlargement in Fig. 11F) and along with the corresponding derivative (Fig. 11E); also in this case, the derivative spectra are shown for the sake of better evidence. At 0.16 V, $LaNiO_3$ shows an edge shifting towards lower energies compared to the pristine material, which is indicative of a partial reduction of Ni at this potential: the spectrum of metallic Ni is extremely different [78], and therefore this reduction can only ascribed to the formation of Ni(II) on the surface, The spectra at the different potentials look very similar, with the remarkable exception of a small shift of the edge energy position towards higher energies, which is increasing in intensity, going to more positive (anodic) potentials. We want here to stress that the shift of the edge energy position is small, but still detectable. This is because we preferred to study a sample whose structural and morphological features are close to those required for future industrial application, rather than being optimized for XAS experiments.

Correspondingly, a shoulder in the derivative spectra at ca. 8348.5 eV increases in amplitude, reaching the larger value at 1.6 V, where the OER is ongoing. It is worth noting here that XAS is bulk sensitive technique, and that the probed depth at the Ni K-edge in the $LaNiO_3$ catalyst can be estimated to be around few microns. In addition, in the CV, cathodic and anodic peaks are observed at about 1.3 V and 1.4 V (vs RHE), which are ascribed to the Ni(II)/Ni(III) couple. Therefore, we can attribute all our experimental finding to the formation of a surface layer of a Ni(II) compound, possibly $Ni(OH)_2$, at 0.16 V. This layer, going to anodic potentials, is oxidized to NiOOH, possibly forming active Ni(III) sites at the surface, and then the OER can proceed via these sites. It should be noted that the fraction of Ni involved in this reaction can be estimated by relating the shift observed in Fig. 11F with the shift between the edge energy position of NiO and β-NiOOH, which in turn amounts to *ca.* 2 eV. A fraction of ca. 10% of Ni is obtained, which is in excellent agreement with the values reported above and obtained via peak integration of the CV plots and that confirms the existence of a defective shell around the particles, notwithstanding the partial deactivation observed in Fig. 10. According to these last results, the partial deactivation can be thus associated to a partial loss of the less adherent particles from the rotating electrode, due to the mechanical action of oxygen bubbles.

The formation of a Ni(III) containing layer is confirmed by the $\Delta\mu$ spectra reported in Fig. 11G. Here the $\Delta\mu$ signal is obtained by subtracting to the spectra at each of the potential, the spectrum at −0.16 V used as a reference. The negative peak, increasing in amplitude going to more positive potential, confirms the shift of the edge to higher energies.

3.5. Surface disorder

Recalling that XANES is also a probe for high-order correlation functions between the photoabsorber and the neighboring, the XANES spectra reported above show that the catalyst is stable in all the

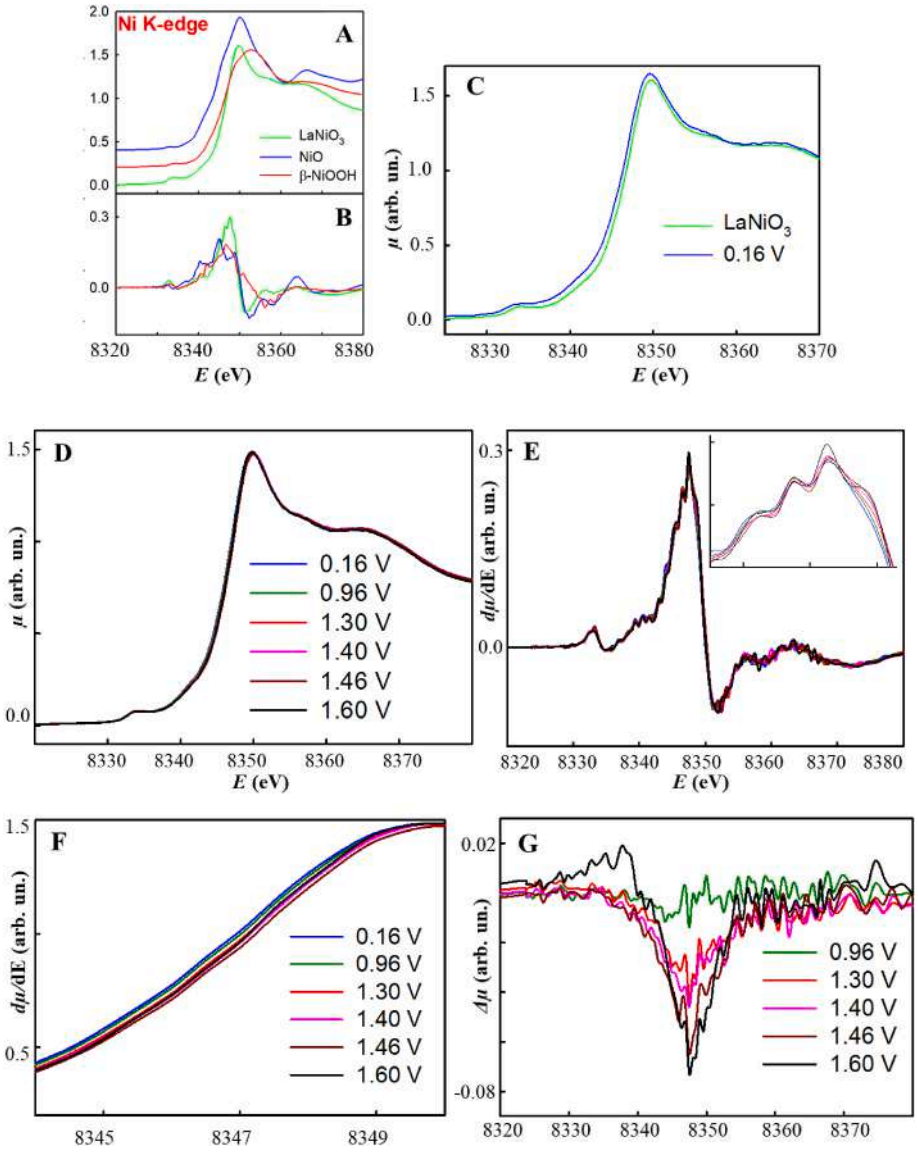

Fig. 11. Ni K-edge XANES spectra and relevant derivative of pristine $LaNiO_3$ (**A - B**), compared with a spectrum of the material at 0.16 V (**C**), and of the material under operando conditions at different potentials **D** (enlargement in panel **F**). In **A** the spectra of NiO and NiOOH are shown for reference of the edge position of Ni(II) and Ni(III), and the spectra are shifted along the y axis for better clarity. The derivative spectra reported in **A** and **D** are shown in the panels **B** and **F**, respectively. The panel **G** shows the Δμ spectra obtained by subtracting at the spectra at each of the potential the spectrum at −0.16 V used as a reference.

investigated conditions.

A confirmation of this conclusion can be obtained by the EXAFS spectra shown in Fig. 12A and Fourier Transform (FT) shown in Fig. 12B. The different spectra refer to cathodic (0.16 V) and anodic conditions (1.46 V). Oxygen bubble formation at potentials larger than 1.46 V did not allow the collection of EXAFS spectra without disturbing spikes at more anodic conditions. The EXAFS data can be fitted against a theoretical model, with R_j (radial distance of the j-th coordination shell from the photo-absorber) and σ_j^2 (variance in R_j) as fitting parameters. We remind here that the EXAFS FT is similar to a radial distribution function around the photo-absorber. The fitting parameters are therefore shown in Table 2, where the crystallographic distances, as calculated from the crystal structure [58], are also reported for reference. It can be noted that: i) the agreement between the EXAFS distances and the crystallographic distances is of good quality, and ii) there are no significant variations in the parameters in all the conditions, apart from a small increase in the EXAFS Debye-Waller factors (σ^2), which may be attributed to a small increase in the disorder in the local chemical environment of Ni. It is then concluded that the crystal structure of $LaNiO_3$ is stable during the water splitting reaction, both in anodic and cathodic investigated potentials [0.16 V–0.96 V – 1.3 V–1.4 V – 1.46 V–1.6 V (vs RHE)].

It can be observed that the OER activity of $LaNiO_3$ has a strong correlation with the corresponding crystalline structure and surface transformation. In $LaNiO_3$, Ni(III) cations are stabilized in the bulk of the perovskite structure, although this is maybe no longer valid at the surface, particularly at the oxide aqueous interface [79]. The surface composition of perovskite oxides, in contact with alkaline solutions, reasonably forms a thin hydrate layer that can be attributed to the formation of a Ni(II) compound, likely $Ni(OH)_2$, under cathodic potential. The layer is subsequently re-oxidized, under anodic potentials, forming fresh Ni(III) sites which are probably the active sites for adsorption and for the OER reaction [34].

Baeumer et al. derived a strong relationship between surface transformation, surface composition and OER activity in $LaNiO_3$ films. They demonstrated the tunability of surface transformation of the $LaNiO_3$ epitaxial thin films by modifying a single atomic layer at the surface showing that the Ni termination is significantly more active than the La

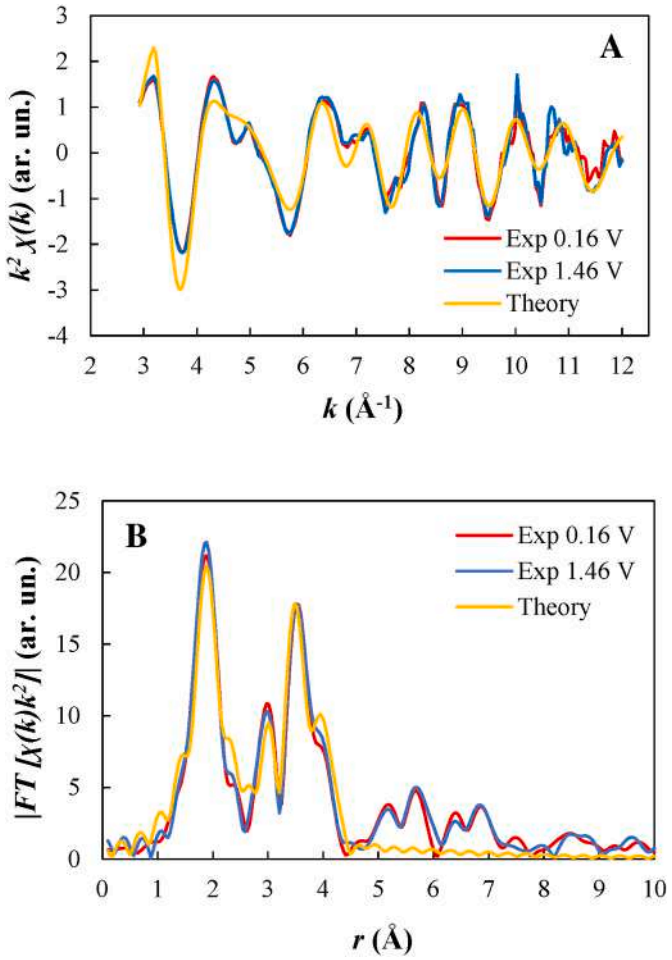

Fig. 12. A) EXAFS spectra in different operando conditions and **B)** the relevant Fourier Transform.

termination. This difference originates from a thermodynamically stable, Ni oxyhydroxide-type one atomic layer (disordered) surface phase NiO_2 evolved on Ni-terminated surfaces, which is kinetically inaccessible when starting with a La termination [46].

According to the results of the present work, we witness a similar behavior but on a polycrystalline material, where the La- and Ni-terminated are randomly distributed over the particles surface. The structure of the layer, formed on the surface, is likely very disordered, which may explain the increase of the EXAFS Debye-Waller factors with increasing potential. We assume that the change in the oxidation state of Ni, leading to the formation of Ni(II), is confined to the surface, causing a reconstruction of the structure by forming extremely small domains, in agreement with the HR-TEM inspections.

Moreover, structural disorder facilitates the ion diffusion and the charge transfer through amorphous materials [80]: due to the very small crystal size of the nano-domains that are grew in the present case, we can assume that this explanation holds also here. This fact, combined to the low amount of this disordered nano-domains, makes the contribution of the surface hydroxide layer to the EXAFS spectra negligible. Similar considerations can be applied also to the XANES part of the X-ray absorption spectra (reported in Fig. 11): the shift of the edge energy position due to the formation of a surface layer of a Ni(II) compound, possibly $Ni(OH)_2$, accounts for only 10% *ca.* of the total number of Ni atoms, which is in line with the statement that the bulk of the catalyst is stable in all the investigated conditions.

We can therefore conclude that the combined effect of the formation of the thin disordered nano-domains and the robustness of the bulk $LaNiO_3$ catalyst, provide it as excellent electrocatalyst for the OER under alkaline conditions.

4. Conclusions

In this work, $LaNiO_3$ prepared by the simple and inexpensive co-precipitation method, has been explored as a highly promising catalyst material for OER in alkaline condition. In addition, morphological and structural analysis, with a strict electrochemical characterization, allow a proper assessment of $LaNiO_3$ for future industrial electrode fabrication. Remarkably, the material shows excellent OER activity and stands out as the most favorable candidate within the perovskite oxides-based family.

Furthermore, the study assesses the stability of the spectro-electrochemical set-up, ensuring the reliability of the experimental results.

The operando XAS experiments revealed that, under cathodic conditions, a layer of a Ni(II) compound, likely $Ni(OH)_2$, forms at the catalyst surface, and it is subsequently re-oxidized under anodic potentials. The fresh Ni(III) sites at the surface are possibly the active sites for adsorption and for the OER reaction. We were able to observe a surface disorder on the polycrystalline $LaNiO_3$ electrocatalyst and combining experimental results.

HR-TEM analysis effectively confirms a remarkable change in the perovskite surface structure. Specifically, it shows that the surface becomes disorder after the powder is subjected to the OER. Thus, this investigation reveals that the formation of Ni(II) is confined to the surface.

We can conclude that the robustness of the bulk $LaNiO_3$ catalyst combined with the surface disorder afford it as excellent electrode for alkaline water electrolysis, particularly under the specific conditions investigated in this study. $LaNiO_3$'s dual strengths of stability and reactivity make it a promising candidate for advancing the field of sustainable green hydrogen production.

CRediT authorship contribution statement

Giuditta De Amicis: Writing – original draft, Investigation, Data curation. **Anna Testolin:** Writing – review & editing, Supervision, Methodology, Data curation, Conceptualization. **Cristina Cazzaniga:** Methodology, Investigation, Data curation. **Francesco D'Acapito:** Writing – review & editing, Validation, Resources, Methodology, Investigation, Data curation. **Alessandro Minguzzi:** Writing – review & editing, Supervision, Resources, Project administration, Investigation, Data curation, Conceptualization. **Paolo Ghigna:** Writing – review &

Table 2
EXAFS fitting parameters.

E (V vs RHE)	R_1 Ni–O/Å	R_2 Ni–La/Å	R_3 Ni–Ni/Å	σ^2 (Å^2)	σ^2 (Å^2)	σ^2 (Å^2)	R (Å) crystallographic
0.16	1.99(1)	3.34(1)	3.82(2)	0.018(1)	0.009(1)	0.013(2)	
0.96	1.99(1)	3.34(1)	3.82(2)	0.019(2)	0.009(1)	0.014(2)	1.9138 (Ni–O)
1.3	1.99(1)	3.34(1)	3.82(1)	0.017(1)	0.009(1)	0.013(2)	3.2861(Ni–La)
1.46	1.98(1)	3.34(1)	3.82(1)	0.018(1)	0.008(1)	0.013(2)	3.8276 (Ni–Ni)
1.6	2.00(2)	3.36(3)	3.84(3)	0.021(3)	0.011(3)	0.013(3)	

editing, Writing – original draft, Supervision, Project administration, Funding acquisition, Data curation, Conceptualization. **Alberto Vertova:** Writing – review & editing, Supervision, Funding acquisition, Conceptualization.

Declaration of competing interest

The authors declare that they have no known competing financial interests or personal relationships that could have appeared to influence the work reported in this paper.

Acknowledgements

We are thankful to PON "Ricerca e Innovazione" 2014–2020, Azione IV.5 "Dottorati su tematiche green" DM1061–10.08.2021.

G.D.A. gratefully acknowledge the Dipartimento di Chimica of the Università degli Studi di Milano for co-financing the project.

Thanks are given to LISA, a project funded by CNR (project DFM. AD006.072). The experiment was carried out under the IHR project IH-EV-36 with doi of the data: https://doi.esrf.fr/10.15151/ESRF-ES-846305705.

A.M. is grateful to a project funded under the National Recovery and Resilience Plan (NRRP), Mission 4 Component 2 Investment 1.3 - Call for tender No. 341 of March 15, 2022 of Ministero dell'Università e della Ricerca (MUR); funded by the European Union – NextGenerationEU Project code PE0000021, Concession Decree No. 1561 of October 11, 2022 adopted by Ministero dell'Università e della Ricerca (MUR), CUP D43C22003090001, Project title "Network 4 Energy Sustainable Transition – NEST".

AV is grateful to Piano di Sostegno alla Ricerca 2022 (Linea 2A) – Università degli Studi di Milano.

TEM analyses were performed at the TEM facility of the Unitech COSPECT at the University of Milan (Italy).

References

[1] A H Y D R O G E N E C O N O M Y Special section. [n.d].
[2] Rosen MA, Scottf DS. Comparative efficiency assessments for a range of hydrogen production processes, vol. 23; 1998.
[3] Sato S, Lin S-Y, Suzuki Y, Hatano H. Hydrogen production from heavy oil in the presence of calcium hydroxide q. [n.d].
[4] Ajanovic A, Sayer M, Haas R. The economics and the environmental benignity of different colors of hydrogen. Int J Hydrogen Energy 2022;47:24136–54. https://doi.org/10.1016/j.ijhydene.2022.02.094.
[5] Ustolin F, Campari A, Taccani R. An extensive review of liquid hydrogen in transportation with focus on the maritime sector. J Mar Sci Eng 2022;10. https://doi.org/10.3390/jmse10091222.
[6] Miranda R. H2nova FB. Hydrogen from renewable power: technology outlook for the energy transition. 2018.
[7] Man IC, Su HY, Calle-Vallejo F, Hansen HA, Martínez JI, Inoglu NG, et al. Universality in oxygen evolution electrocatalysis on oxide surfaces. ChemCatChem 2011;3:1159–65. https://doi.org/10.1002/cctc.201000397.
[8] Peng S, Gong F, Li L, Yu D, Ji D, Zhang T, et al. Necklace-like multishelled hollow spinel oxides with oxygen vacancies for efficient water electrolysis. J Am Chem Soc 2018;140:13644–53. https://doi.org/10.1021/jacs.8b05134.
[9] Xu H, Yuan J, He G, Chen H. Current and future trends for spinel-type electrocatalysts in electrocatalytic oxygen evolution reaction. Coord Chem Rev 2023;475. https://doi.org/10.1016/j.ccr.2022.214869.
[10] Xu H, Zhao Y, He G, Chen H. Race on engineering noble metal single-atom electrocatalysts for water splitting. Int J Hydrogen Energy 2022;47:14257–79. https://doi.org/10.1016/j.ijhydene.2022.02.152.
[11] Reier T, Nong HN, Teschner D, Schlögl R, Strasser P. Electrocatalytic oxygen evolution reaction in acidic environments – reaction mechanisms and catalysts. Adv Energy Mater 2017;7. https://doi.org/10.1002/aenm.201601275.
[12] Lee Y, Suntivich J, May KJ, Perry EE, Shao-Horn Y. Synthesis and activities of rutile IrO 2 and RuO 2 nanoparticles for oxygen evolution in acid and alkaline solutions. J Phys Chem Lett 2012;3:399–404. https://doi.org/10.1021/jz2016507.
[13] Chu X, Wang L, Li J, Xu H. Strategies for promoting catalytic performance of Ru-based electrocatalysts towards oxygen/hydrogen evolution reaction. Chem Rec 2023;23. https://doi.org/10.1002/tcr.202300013.
[14] Yuan M, Luo J, Xu H, Wang C, Wang Y, Wang Y, et al. Hydrogen evolution reaction catalysis on RuM (M = Ni, Co) porous nanorods by cation etching. J Colloid Interface Sci 2022;624:279–86. https://doi.org/10.1016/j.jcis.2022.05.133.
[15] Owe LE, Tsypkin M, Wallwork KS, Haverkamp RG, Sunde S. Iridium-ruthenium single phase mixed oxides for oxygen evolution: composition dependence of electrocatalytic activity. Electrochim Acta 2012;70:158–64. https://doi.org/10.1016/j.electacta.2012.03.041.
[16] McCrory CCL, Jung S, Peters JC, Jaramillo TF. Benchmarking heterogeneous electrocatalysts for the oxygen evolution reaction. J Am Chem Soc 2013;135:16977–87. https://doi.org/10.1021/ja407115p.
[17] McCrory CCL, Jung S, Ferrer IM, Chatman SM, Peters JC, Jaramillo TF. Benchmarking hydrogen evolving reaction and oxygen evolving reaction electrocatalysts for solar water splitting devices. J Am Chem Soc 2015;137:4347–57. https://doi.org/10.1021/ja510442p.
[18] Kamm B, Gruber PR. Related titles materials for low-temperature fuel cells fuel cells problems and solutions eff icient carbon capture for coal power plants fuel cell science theory, fundamentals, and biocatalysis energy production and storage inorganic chemical strategies for a warming world bioref ineries-industrial processes and products hydrogen and fuel cells fundamentals. Technologies and Applications 2013.
[19] Colli AN, Girault HH, Battistel A. Non-precious electrodes for practical alkaline water electrolysis. Materials 2019;12. https://doi.org/10.3390/ma12081336.
[20] Colli AN, Girault HH, Battistel A. Non-precious electrodes for practical alkaline water electrolysis. Materials 2019;12. https://doi.org/10.3390/ma12081336.
[21] Suen NT, Hung SF, Quan Q, Zhang N, Xu YJ, Chen HM. Electrocatalysis for the oxygen evolution reaction: recent development and future perspectives. Chem Soc Rev 2017;46:337–65. https://doi.org/10.1039/c6cs00328a.
[22] dos Santos PL, Rowley-Neale SJ, Ferrari AGM, Bonacin JA, Banks CE. Ni−Fe (Oxy) hydroxide modified graphene additive manufactured (3D-printed) electrochemical platforms as an efficient electrocatalyst for the oxygen evolution reaction. Chemelectrochem 2019;6:5633–41. https://doi.org/10.1002/celc.201901541.
[23] Yadav DK, Ganesan V, Sonkar PK, Gupta R. Templated synthesis of Nickel−Iron layered double hydroxide for enhanced electrocatalytic water oxidation: towards the development of non-precious-metal catalysts. Chemelectrochem 2017;4:3134–9. https://doi.org/10.1002/celc.201700867.
[24] Li J, Li J, Zhou X, Xia Z, Gao W, Ma Y, et al. Highly efficient and robust nickel phosphides as bifunctional electrocatalysts for overall water-splitting. ACS Appl Mater Interfaces 2016;8:10826–34. https://doi.org/10.1021/acsami.6b00731.
[25] Ren JT, Yao Y, Yuan ZY. Fabrication strategies of porous precious-metal-free bifunctional electrocatalysts for overall water splitting: recent advances. Green Energy Environ 2021;6:620–43. https://doi.org/10.1016/j.gee.2020.11.023.
[26] Cheng W, Wang H, Gu Z, Cao M, He C, Li J, et al. Modulation of the electronic structure of CoP by surface and interface codoping boosts electrocatalytic oxygen evolution reaction. Int J Hydrogen Energy 2024;51:914–21. https://doi.org/10.1016/j.ijhydene.2023.10.256.
[27] Lu X, Wang T, Cao M, Cheng W, Yang H, Xu H, et al. Homogeneous NiMoO4–Co (OH)2 bifunctional heterostructures for electrocatalytic oxygen evolution and urea oxidation reaction. Int J Hydrogen Energy 2023;48:34740–9. https://doi.org/10.1016/j.ijhydene.2023.04.257.
[28] Kim N-I, Sa YJ, Yoo TS, Choi SR, Afzal RA, Choi T, et al. Oxygen-deficient triple perovskites as highly active and durable bifunctional electrocatalysts for oxygen electrode reactions. 2018.
[29] Gozzo CB, Soares MRS, Sczancoski JC, Nogueira IC, Leite ER. Investigation of the electrocatalytic performance for oxygen evolution reaction of Fe-doped lanthanum nickelate deposited on pyrolytic graphite sheets. Int J Hydrogen Energy 2019;44:21659–72. https://doi.org/10.1016/j.ijhydene.2019.06.109.
[30] Liu D, Zhou P, Bai H, Ai H, Du X, Chen M, et al. Development of perovskite oxide-based electrocatalysts for oxygen evolution reaction. Small 2021;17.
[31] Wu Y, Wang T, Zhang Y, Xin S, He X, Zhang D, et al. Electrocatalytic performances of g-C 3 N 4 -LaNiO 3 composite as bi-functional catalysts for lithium-oxygen batteries. Sci Rep 2016;6. https://doi.org/10.1038/srep24314.
[32] Du Z, Yang P, Wang L, Lu Y, Goodenough JB, Zhang J, et al. Electrocatalytic performances of LaNi1-xMgxO 3 perovskite oxides as bi-functional catalysts for lithium air batteries. J Power Sources 2014;265:91–6. https://doi.org/10.1016/j.jpowsour.2014.04.096.
[33] Otagawa T, Bockris M. Lanthanum nickelate as electrocatalyst: oxygen evolution. [n.d].
[34] Ding H, Liu H, Chu W, Wu C, Xie Y. Structural transformation of heterogeneous materials for electrocatalytic oxygen evolution reaction. Chem Rev 2021;121:13174–212. https://doi.org/10.1021/acs.chemrev.1c00234.
[35] Guo T, Li L, Wang Z. Recent development and future perspectives of amorphous transition metal-based electrocatalysts for oxygen evolution reaction. Adv Energy Mater 2022;12. https://doi.org/10.1002/aenm.202200827.
[36] Scholz J, Risch M, Wartner G, Luderer C, Roddatis V, Jooss C. Tailoring the oxygen evolution activity and stability using defect chemistry. Catalysts 2017;7. https://doi.org/10.3390/catal7050139.
[37] Achilli E, Minelli S, Casale I, He X, Agostini G, Spinolo G, et al. Determining the proton diffusion coefficient in highly hydrated iridium oxide films by energy dispersive X-ray absorption spectroscopy. Electrochim Acta 2023;444:142017. https://doi.org/10.1016/j.electacta.2023.142017.
[38] Cherevko S, Reier T, Zeradjanin AR, Pawolek Z, Strasser P, Mayrhofer KJJ. Stability of nanostructured iridium oxide electrocatalysts during oxygen evolution reaction in acidic environment. Electrochem Commun 2014;48:81–5. https://doi.org/10.1016/j.elecom.2014.08.027.
[39] Cherevko S, Geiger S, Kasian O, Mingers A, Mayrhofer KJJ. Oxygen evolution activity and stability of iridium in acidic media. Part 2. - electrochemically grown hydrous iridium oxide. J Electroanal Chem 2016;774:102–10. https://doi.org/10.1016/j.jelechem.2016.05.015.
[40] Geiger S, Kasian O, Ledendecker M, Pizzutilo E, Mingers AM, Fu WT, et al. The stability number as a metric for electrocatalyst stability benchmarking. Nat Catal 2018;1:508–15. https://doi.org/10.1038/s41929-018-0085-6.

[41] Fierro S, Kapałka A, Comninellis C. Electrochemical comparison between IrO2 prepared by thermal treatment of iridium metal and IrO2 prepared by thermal decomposition of H2IrCl6 solution. Electrochem Commun 2010;12:172–4. https://doi.org/10.1016/j.elecom.2009.11.018.
[42] Smith RDL, Prévot MS, Fagan RD, Zhang Z, Sedach PA, Siu MKJ, et al. Photochemical route for accessing amorphous metal oxide materials for water oxidation catalysis. Science 2013;340:60–3. https://doi.org/10.1126/science.1233638 (1979).
[43] Elmaalouf M, Odziomek M, Duran S, Gayrard M, Bahri M, Tard C, et al. The origin of the high electrochemical activity of pseudo-amorphous iridium oxides. Nat Commun 2021;12:1–10. https://doi.org/10.1038/s41467-021-24181-x.
[44] Bergmann A, Martinez-Moreno E, Teschner D, Chernev P, Gliech M, De Araújo JF, et al. Reversible amorphization and the catalytically active state of crystalline Co3O4 during oxygen evolution. Nat Commun 2015;6:1–9. https://doi.org/10.1038/ncomms9625.
[45] Ardizzone S, Bianchi CL, Cappelletti G, Ionita M, Minguzzi A, Rondinini S, et al. Composite ternary SnO2-IrO2-Ta2O5 oxide electrocatalysts. J Electroanal Chem 2006;589:160–6. https://doi.org/10.1016/j.jelechem.2006.02.004.
[46] Baeumer C, Li J, Lu Q, Liang AYL, Jin L, Martins HP, et al. Tuning electrochemically driven surface transformation in atomically flat LaNiO3 thin films for enhanced water electrolysis. Nat Mater 2021;20:674–82. https://doi.org/10.1038/s41563-020-00877-1.
[47] Feng CH, Li QS, Liu CM, Deng Y, Guo L. Synthesis of perovskite-type $LaMnO_3$ under hydrothermal conditions. Mater Sci Forum 2005;475–479:4051–4. https://doi.org/10.4028/www.scientific.net/msf.475-479.4051.
[48] Malara F, Fracchia M, Kmentová H, Psaro R, Vertova A, Oliveira De Souza D, et al. Direct observation of photoinduced higher oxidation states at a semiconductor/electrocatalyst junction. ACS Catal 2020;10:10476–87. https://doi.org/10.1021/acscatal.0c02789.
[49] Minguzzi A, Locatelli C, Lugaresi O, Achilli E, Cappelletti G, Scavini M, et al. Easy accommodation of different oxidation states in iridium oxide nanoparticles with different hydration degree as water oxidation electrocatalysts. ACS Catal 2015;5:5104–15. https://doi.org/10.1021/acscatal.5b01281.
[50] Minguzzi A, Naldoni A, Lugaresi O, Achilli E, D'Acapito F, Malara F, et al. Observation of charge transfer cascades in α-Fe2O3/IrOx photoanodes by operando X-ray absorption spectroscopy. Phys Chem Chem Phys 2017;19:5715–20. https://doi.org/10.1039/c6cp08053g.
[51] Ellis DS, Tsyganok A, Ghigna P, Minguzzi A, Naldoni A, Murzin V, et al. Operando X-ray Absorption Spectroscopy (XAS) observation of photoinduced oxidation in FeNi (Oxy)hydroxide overlayers on hematite (α-Fe2O3) photoanodes for solar water splitting. Langmuir 2020;36:11564–72. https://doi.org/10.1021/acs.langmuir.0c02065.
[52] Baran T, Fracchia M, Vertova A, Achilli E, Naldoni A, Malara F, et al. Operando and time-resolved X-ray absorption spectroscopy for the study of photoelectrode architectures. Electrochim Acta 2016;207:16–21. https://doi.org/10.1016/j.electacta.2016.04.153.
[53] Minguzzi A, Lugaresi O, Achilli E, Locatelli C, Vertova A, Ghigna P, et al. Observing the oxidation state turnover in heterogeneous iridium-based water oxidation catalysts. Chem Sci 2014;5:3591–7. https://doi.org/10.1039/c4sc00975d.
[54] Achilli E, Minguzzi A, Visibile A, Locatelli C, Vertova A, Naldoni A, et al. 3D-printed photo-spectroelectrochemical devices for in situ and in operando X-ray absorption spectroscopy investigation. J Synchrotron Radiat 2016;23:622–8. https://doi.org/10.1107/S1600577515024480.
[55] Li Z, Yang H, Cheng W, Tian L. Recent progress of in situ/operando characterization techniques for electrocatalytic energy conversion reaction. Chin Chem Lett 2024;35. https://doi.org/10.1016/j.cclet.2023.109237.
[56] Gutiérrez-Tarriño S, Portorreal-Bottier A, Trasobares S, Calvente JJ, Calvino JJ, Olloqui-Sariego JL, et al. Understanding the potential-induced activation of a cobalt MOF electrocatalyst for the oxygen evolution reaction. Appl Surf Sci 2023;623. https://doi.org/10.1016/j.apsusc.2023.157001.
[57] Elmaalouf M, Odziomek M, Duran S, Gayrard M, Bahri M, Tard C, et al. The origin of the high electrochemical activity of pseudo-amorphous iridium oxides. Nat Commun 2021;12. https://doi.org/10.1038/s41467-021-24181-x.
[58] Matienzo DJD, Kutlusoy T, Divanis S, di Bari C, Instuli E. Benchmarking perovskite electrocatalysts' oer activity as candidate materials for industrial alkaline water electrolysis. Catalysts 2020;10:1–9. https://doi.org/10.3390/catal10121387.
[59] Schmidt J, Gasteiger HA, Stab GD, Urban PM, Koib DM, Behm° RJ. Characterization of high-surface-area electrocatalysts using a rotating Disk electrode configuration, vol. 145; 1998.
[60] Minguzzi A, Fan FRF, Vertova A, Rondinini S, Bard AJ. Dynamic potential-pH diagrams application to electrocatalysts for water oxidation. Chem Sci 2012;3:217–29. https://doi.org/10.1039/c1sc00516b.
[61] D'Acapito F, Lepore GO, Puri A, Laloni A, La Manna F, Dettona E, et al. The LISA beamline at ESRF. J Synchrotron Radiat 2019;26:551–8. https://doi.org/10.1107/S160057751801843X.
[62] Malara F, Fracchia M, Kmentová H, Psaro R, Vertova A, Oliveira De Souza D, et al. Direct observation of photoinduced higher oxidation states at a semiconductor/electrocatalyst junction. ACS Catal 2020;10:10476–87. https://doi.org/10.1021/acscatal.0c02789.
[63] Ravel B, Newville M. ARTEMIS, hephaestus: data analysis for X-ray absorption spectroscopy using IFEFFIT. J Synchrotron Radiat 2005;12:537–41. https://doi.org/10.1107/S0909049505012719.
[64] Newville M. IFEFFIT: interactive XAFS analysis and FEFF fitting. 2001.
[65] Maiwald MM, Dardenne K, Rothe J, Skerencak-Frech A, Panak PJ. Thermodynamics and structure of neptunium(V) complexes with formate. Spectroscopic and theoretical study. Inorg Chem 2020;59:6067–77. https://doi.org/10.1021/acs.inorgchem.0c00054.
[66] Pereñíguez R, González-DelaCruz VM, Holgado JP, Caballero A. Synthesis and characterization of a LaNiO3 perovskite as precursor for methane reforming reactions catalysts. Appl Catal, B 2010;93:346–53. https://doi.org/10.1016/j.apcatb.2009.09.040.
[67] Gorlin Y, Jaramillo TF. A bifunctional nonprecious metal catalyst for oxygen reduction and water oxidation. J Am Chem Soc 2010;132:13612–4. https://doi.org/10.1021/ja104587v.
[68] Minguzzi A, Fan FRF, Vertova A, Rondinini S, Bard AJ. Dynamic potential-pH diagrams application to electrocatalysts for water oxidation. Chem Sci 2012;3:217–29. https://doi.org/10.1039/c1sc00516b.
[69] Suen NT, Hung SF, Quan Q, Zhang N, Xu YJ, Chen HM. Electrocatalysis for the oxygen evolution reaction: recent development and future perspectives. Chem Soc Rev 2017;46:337–65. https://doi.org/10.1039/c6cs00328a.
[70] O J, Bockris M, Otagawa T. Mechanism of oxygen evolution on perovskites, vol. 57; 1983.
[71] Bockris JOM. Kinetics of activation controlled consecutive electrochemical reactions: anodic evolution of oxygen. J Chem Phys 1956;24:817–27. https://doi.org/10.1063/1.1742616.
[72] Srinivasa N, Hughes JP, Adarakatti PS, Manjunatha C, Rowley-Neale SJ, Ashoka S, et al. Facile synthesis of Ni/NiO nanocomposites: the effect of Ni content in NiO upon the oxygen evolution reaction within alkaline media. RSC Adv 2021;11:14654–64. https://doi.org/10.1039/d0ra10597j.
[73] Silva VD, Simões TA, Grilo JPF, Medeiros ES, Macedo DA. Impact of the NiO nanostructure morphology on the oxygen evolution reaction catalysis. J Mater Sci 2020;55:6648–59. https://doi.org/10.1007/s10853-020-04481-1.
[74] Costentin C, Drouet S, Robert M, Savéant JM. Turnover numbers, turnover frequencies, and overpotential in molecular catalysis of electrochemical reactions. Cyclic voltammetry and preparative-scale electrolysis. J Am Chem Soc 2012;134:11235–42. https://doi.org/10.1021/ja303560c.
[75] Minguzzi A, Locatelli C, Cappelletti G, Bianchi CL, Vertova A, Ardizzone S, et al. Designing materials by means of the cavity-microelectrode: the introduction of the quantitative rapid screening toward a highly efficient catalyst for water oxidation. J Mater Chem 2012;22:8896–902. https://doi.org/10.1039/c2jm15750k.
[76] Lu X, Zhao C. Electrodeposition of hierarchically structured three-dimensional nickel-iron electrodes for efficient oxygen evolution at high current densities. Nat Commun 2015;6. https://doi.org/10.1038/ncomms7616.
[77] Nishio K, Molla S, Okugaki T, Nakanishi S, Nitta I, Kotani Y. Effects of carbon on oxygen reduction and evolution reactions of gas-diffusion air electrodes based on perovskite-type oxides. J Power Sources 2015;298:236–40. https://doi.org/10.1016/j.jpowsour.2015.08.070.
[78] Spanu D, Minguzzi A, Recchia S, Shahvardanfard F, Tomanec O, Zboril R, et al. An operando x-ray absorption spectroscopy study of a NiCu-TiO2 photocatalyst for H2 evolution. ACS Catal 2020;10:8293–302. https://doi.org/10.1021/acscatal.0c01373.
[79] O'Sullivan EJM, Calvo EJ. Reactions at metal oxide electrodes. Compr Chem Kinet 1988;27:247–360. https://doi.org/10.1016/S0069-8040(08)70017-7.
[80] Guo T, Li L, Wang Z. Recent development and future perspectives of amorphous transition metal-based electrocatalysts for oxygen evolution reaction. Adv Energy Mater 2022;12. https://doi.org/10.1002/aenm.202200827.